Editors' Suggestion

Time-Dependent Magnetic Flux in Devices for Circuit Quantum Electrodynamics

Jacob Bryon,[1,*] D.K. Weiss,[2,†] Xinyuan You,[3,‡] Sara Sussman,[4] Xanthe Croot,[4] Ziwen Huang,[2,‡] Jens Koch,[2,5] and Andrew A. Houck[1]

[1] *Department of Electrical Engineering, Princeton University, Princeton, New Jersey 08540, USA*
[2] *Department of Physics and Astronomy, Northwestern University, Evanston, Illinois 60208, USA*
[3] *Graduate Program in Applied Physics, Northwestern University, Evanston, Illinois 60208, USA*
[4] *Department of Physics, Princeton University, Princeton, New Jersey 08540, USA*
[5] *Center for Applied Physics and Superconducting Technologies, Northwestern University, Evanston, Illinois 60208, USA*

(Received 6 September 2022; revised 6 February 2023; accepted 8 February 2023; published 9 March 2023)

Recent theoretical work has highlighted that quantizing a superconducting circuit in the presence of time-dependent flux $\Phi(t)$ generally produces Hamiltonian terms proportional to $d\Phi/dt$ unless a special allocation of the flux across inductive terms is chosen. Here, we present an experiment probing the effects of a fast flux ramp applied to a heavy-fluxonium circuit. The experiment confirms that naïve omission of the $d\Phi/dt$ term leads to theoretical predictions inconsistent with experimental data. Experimental data are fully consistent with recent theory that includes the derivative term or equivalently uses "irrotational variables" that uniquely allocate the flux to properly eliminate the $d\Phi/dt$ term.

DOI: 10.1103/PhysRevApplied.19.034031

I. INTRODUCTION

The use of time-dependent flux is ubiquitous in the context of circuit quantum electrodynamics. Flux modulation is utilized, for example, for realizing fast two-qubit gates with transmons [1–4], demonstrating universal stabilization of arbitrary single-qubit states between a qubit and a resonator [5,6], sweet-spot engineering of transmons using two-tone flux modulation [7], enhancing fluxonium coherence via Floquet engineering [8,9], and realizing fast gates on fluxonium qubits [10–14]. Given the importance of flux modulation for the control of superconducting circuits, it is critical to accurately model time-dependent flux in circuit Hamiltonians.

Recent theory work has investigated the treatment of time-dependent external flux in superconducting circuits both for lumped-element models [15], and for distributed geometries [16,17]. Considering the lumped-element model of the fluxonium circuit as an example, external flux is usually allocated either to the inductor term in the Hamiltonian [18] or to the Josephson junction term [19–21]. Under static conditions, both choices are related by a constant variable shift and naturally result in identical predictions. This ceases to be true in the context of time-dependent flux $\Phi(t)$. In the case of fluxonium, the junction allocation of time-dependent external flux yields an additional term in the Hamiltonian which is proportional to the time derivative of the external flux, $d\Phi/dt$ [15]. By contrast, the inductor allocation of external flux produces the more familiar form of the Hamiltonian in which the $d\Phi/dt$ term is absent, making this special choice valid in both time-independent and time-dependent scenarios.

In this work, we experimentally test and compare predictions for the dynamics under time-dependent flux, based on the inductor allocation and the incomplete junction allocation in which the additional $d\Phi/dt$ term is incorrectly omitted. Beginning with a flux bias Φ_a at or near the half-flux sweet spot, we apply a fast flux pulse to ramp to a new flux point Φ_b. We then read out the occupation probability in the ground and first excited states, and compare the experimental data to theory based on the inductor allocation and the incomplete junction allocation. We find excellent agreement with theory based on the correct inductor allocation, and poor agreement with the incomplete junction allocation. These findings provide experimental evidence for the theory of circuit

*jbryon@princeton.edu
†Present address: Yale Quantum Institute, Yale University, New Haven, Connecticut 06511, USA
‡Present address: Superconducting Quantum Materials and Systems Center, Fermi National Accelerator Laboratory (FNAL), Batavia, IL 60510, USA

quantization presented in Ref. [15], and highlight the importance of using irrotational variables when working with time-dependent flux.

II. THEORY

In the literature, the fluxonium Hamiltonian is found in the following two forms [18–21]:

$$H_1 = 4E_C n^2 - E_J \cos(\varphi) + \frac{1}{2}E_L(\varphi - \phi)^2, \qquad (1)$$

$$H_2 = 4E_C n^2 - E_J \cos(\varphi + \phi) + \frac{1}{2}E_L\varphi^2. \qquad (2)$$

Here, E_C, E_L, and E_J denote the usual charging, inductive, and Josephson energies, and the phase and charge operators φ and n are canonically conjugate and obey $[\varphi, n] = i$. We have further defined the reduced external flux $\phi = 2\pi\Phi/\Phi_0$ in terms of the applied magnetic flux Φ and superconducting flux quantum $\Phi_0 = h/2e$. The key difference between Eqs. (1) and (2) is the allocation of the external flux ϕ to the inductive terms in the Hamiltonian: flux is allocated to the inductor term in H_1, but to the junction term in H_2. When the external flux is static, both choices are equivalent [22,23]. However, in the presence of time-dependent flux $\phi \to \phi(t)$, this equivalence no longer holds. Following Refs. [15,16], the proper handling of time-dependent flux must already occur at the level of the classical Lagrangian. In short, the fluxonium circuit involves two branch variables: the branch variable φ_J of the junction and the branch variable φ_L of the inductor (see Fig. 1). Fluxoid quantization [24] now imposes semiholonomic constraints for both the generalized coordinates and the velocities [25]:

$$\varphi_J + \varphi_L = \phi(t), \quad \dot{\varphi}_J + \dot{\varphi}_L = \dot{\phi}(t). \qquad (3)$$

From here, one proceeds by eliminating one of the variables and its time derivative. This leads to a Lagrangian describing a single degree of freedom which will generally involve a term proportional to $\dot{\phi}(t)$. One choice of variables (also known as the irrotational variables in Ref. [15]) succeeds in the elimination of that term. For the fluxonium circuit this special choice leads to the Hamiltonian

$$H_1(t) = 4E_C n^2 - E_J \cos(\varphi) + \frac{1}{2}E_L[\varphi - \phi(t)]^2, \qquad (4)$$

where the time-dependent external flux is fully allocated to the inductor term. By contrast, if we force the time-dependent external flux to be allocated with the junction,

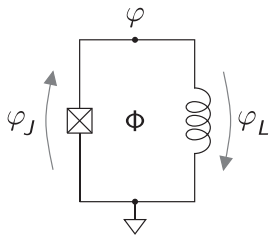

FIG. 1. The fluxonium circuit is formed by a Josephson junction and an inductor with respective branch variables φ_J, φ_L. The bottom node is chosen as the reference ground while the top node is associated with the node variable φ. The junction and inductor form a loop which may be threaded by an external flux Φ.

we obtain the Hamiltonian

$$H_2(t) = 4E_C n^2 - 2en\dot{\Phi} - E_J \cos[\varphi + \phi(t)] + \frac{1}{2}E_L(\varphi)^2. \qquad (5)$$

This includes the aforementioned time-derivative term. Thus, the naïve generalization of Eq. (1) for $\phi \to \phi(t)$ is correct [cf. Eq. (4)], while simply taking $\phi \to \phi(t)$ in Eq. (2) is incorrect [cf. Eq. (5)]. The central goal and main result of this paper are the experimental verification of this theory.

The effects of a fast flux pulse provide an ideal testbed for comparing predictions based on the inductor allocation versus the incomplete junction allocation. (We will not discuss further the complete and correct form of junction allocation [Eq. (5)], which must give results identical to those obtained from the inductor allocation of the time-dependent flux.) We devise a simple experiment based on dc flux-biasing the qubit near the half-flux sweet spot, then ramping quickly to a new value of flux, and finally performing readout. To see how the two allocation methods will yield different predictions, consider the following. At the initial and final flux bias points Φ_a and Φ_b, respectively, we write the Hamiltonian in its eigenbasis

$$H(\Phi_\mu) = \sum_j \omega_{j,\mu}|j_\mu\rangle\langle j_\mu|, \quad \mu = a, b. \qquad (6)$$

While both allocations give the same results for eigenenergies $\omega_{j,\mu}$ and expectation values [15], the wave functions $|j_\mu\rangle$ do depend on the flux allocation, as we will discuss below.

At time $t = t_0$ with the system in state $|\psi_{\text{initial}}\rangle$, we imagine switching on a fast, nonadiabatic flux pulse which ramps from Φ_a to the final flux point Φ_b (Fig. 2). Within the sudden approximation [26], the quantum state remains unchanged under a rapid flux pulse. The probability of

occupying an $H(\Phi_b)$-eigenstate $|m_b\rangle$ at times later than t_0 is

$$p_m = |\langle m_b|\psi_{\text{initial}}\rangle|^2. \tag{7}$$

Crucially, the overlap in Eq. (7) is altered if the $d\Phi/dt$ term is erroneously omitted for the junction allocation of the external flux. This finding can be observed straightforwardly in Fig. 3. In Fig. 3(a) we show the qubit's lowest-lying wave functions at $\Phi_a/\Phi_0 = 0.5$. In Figs. 3(b) and 3(c) we compare the wave functions at $\Phi_b/\Phi_0 = 0.812$ to those at $\Phi_a/\Phi_0 = 0.5$ for inductor and junction allocations, respectively. We observe, for example, that the overlap of the ground state at Φ_b with the ground state at Φ_a in the case of inductor allocation is larger than for the incomplete junction allocation, due to the shift in minimum locations. Because the wave functions are centered around potential minima, the differing shifts in the minimum locations lead to quantitatively different results.

To see why the minimum shifts should differ based on the flux allocation, consider the following discussion of the change in minimum location based on a small flux shift. (The following analysis offers intuition but does not yield quantitatively accurate results for the experiment conducted here, as the flux shift is not "small.") Consider the dc flux ϕ and the associated global minimum of the potential energy $\bar{\varphi}$. (In the case of degenerate minima, select either one of them.) Suppose now we add a perturbation $\phi \to \phi + \delta\phi$. Solving for the perturbed minimum location $\bar{\varphi} + \delta\varphi$, we obtain in the case of inductor allocation

$$\delta\varphi = \frac{E_L}{E_L + E_J\cos(\bar{\varphi})}\delta\phi \approx \frac{E_L}{E_J}\delta\phi, \tag{8}$$

and in the case of junction allocation

$$\delta\varphi = \frac{E_J\cos(\bar{\varphi} - \phi)}{E_L + E_J\cos(\bar{\varphi} - \phi)}\delta\phi \approx \delta\phi. \tag{9}$$

We have neglected quadratic corrections, and the approximation holds in the parameter regime $E_J \gg E_L$ typical of fluxonium qubits. Thus, the shift is large for the junction allocation compared to the inductor allocation of the flux. (We emphasize that the complete junction allocation not omitting the $d\Phi/dt$ term yields the same results as the inductor allocation.)

Choosing initial flux biases near half-flux is advantageous for two reasons. First, the nature of the eigenstates $|j_a\rangle$ changes dramatically in the vicinity of the half-flux point. For $\Phi/\Phi_0 = 0.5$ the qubit eigenstates are delocalized across the two degenerate minima (see Fig. 3). Moving away from half-flux, the eigenstates quickly localize in a single minimum. Thus, small shifts in the starting flux bias Φ_a can lead to large changes in the overlaps. Second,

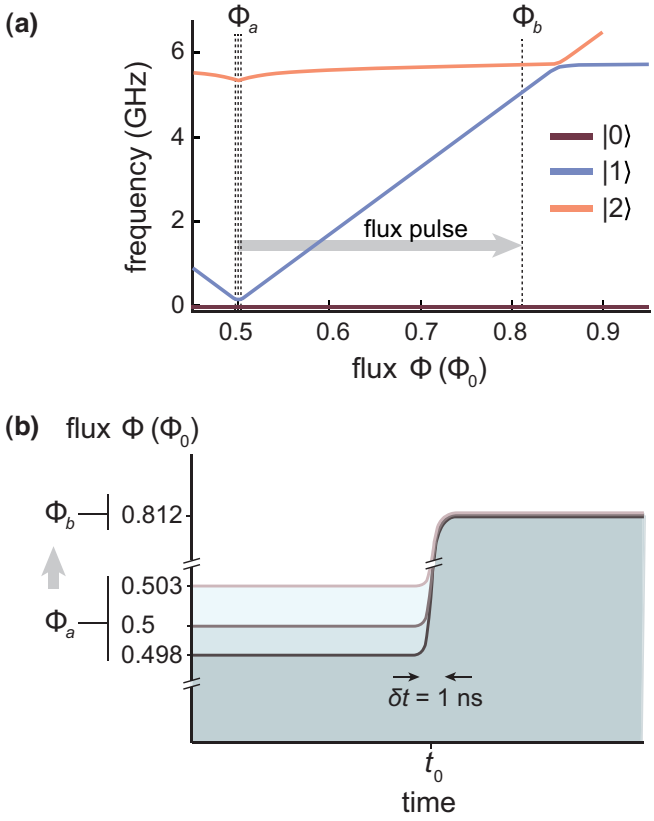

FIG. 2. (a) Fluxonium energy spectrum as a function of external flux, showing the first three energy levels. Vertical lines indicate flux bias points used in the experiment. Starting flux biases are close to half-flux, $\Phi_a/\Phi_0 \in [0.498, 0.503]$. The final flux bias reached after the pulse is $\Phi_b/\Phi_0 = 0.812$. (b) External flux as a function of time for the sudden approximation experiment. The dc flux of the external magnet can be precisely tuned to set the starting point near half-flux. Then, using the QICK qubit controller, we generate a step function with a 1 ns rising edge to drive external flux via the on-chip flux bias line. We calibrate the drive power such that we always drive to $\Phi_b/\Phi_0 = 0.812$. By tuning the starting flux point we are able to change the initial state and thus the final state occupation probability.

thanks to the small energy splitting at the half-flux point, the nonadiabaticity required for the sudden-approximation description [26] is readily achieved with pulse rising-edge times less than about 10 ns. We fix the final flux value Φ_b away from half-flux to a location where we can perform high-fidelity readout and where the charge matrix element is large enough between the lowest two levels to drive a fast π-pulse [28]. There is a range of flux values that satisfy these conditions below the $|1\rangle$–$|2\rangle$ state avoided crossing (see Fig. 2 near $\Phi/\Phi_0 = 0.85$). Here, we choose $\Phi_b/\Phi_0 = 0.812$. Measuring the occupation probability at the final flux value as a function of the starting flux values yields a range over which we can compare theory predictions with experimental data.

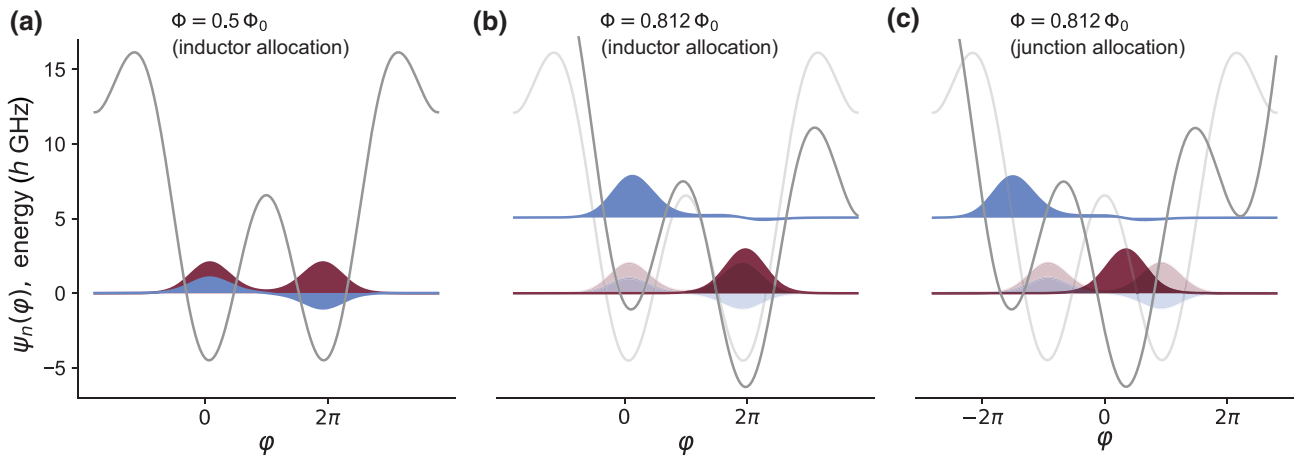

FIG. 3. Fluxonium eigenstates as a function of flux. (a) The two lowest-energy fluxonium eigenstates at the half-flux sweet spot. (b),(c) The two lowest-energy fluxonium eigenstates at $\Phi/\Phi_0 = 0.812$ using the (b) inductor and (c) junction allocation of the flux. The potential and eigenstates for half-flux are transparently overlaid. While the eigenenergies do not depend on the allocation of the external flux to different terms in the fluxonium Hamiltonian, the shifts of the potential minima and thus the relative wave function locations in φ space do depend on it. Since final occupation probability depends on wave function overlaps, the incomplete junction allocation and inductor allocation produce different predictions. Circuit parameters used are $E_J/h = 6.49$ GHz, $E_C/h = 0.755$ GHz, $E_L/h = 0.445$ GHz. Wave function plots are generated using `scQubits` [27].

III. METHODS

In this work we use a two-dimensional fluxonium circuit capacitively coupled to a coplanar waveguide (CPW) for both addressing and reading out the qubit [28]. The inductor is formed by a large array of 159 Josephson junctions. All junctions are made with Dolan bridges. To assist in reading out the qubit state we use a traveling-wave parametric amplifier [29]. The external flux is controlled by both an on-chip flux line that runs near the loop of the fluxonium circuit and a global external magnet. The global magnet is used to set the initial dc flux point Φ_a, while the on-chip flux line is used to drive a step function flux pulse to the final point Φ_b. The device is cooled and measured in a dilution refrigerator with a base temperature of 15 mK. We perform two-tone spectroscopy measurements [30], and fit the data to determine the qubit parameters: $E_J/h = 6.49$ GHz, $E_C/h = 0.755$ GHz, $E_L/h = 0.445$ GHz, CPW cavity frequency 7.39 GHz and linewidth 400 kHz, qubit-cavity coupling strength 110 MHz. At half-flux, the frequency splitting between the ground and first excited states is 20 MHz. Due to the low qubit frequency relative to the ambient temperature, both relaxation and excitation occur with nearly the same rate, with characteristic times $T_1 = 6.2 \pm 0.2$ μs. At the second flux point $\Phi = 0.812\ \Phi_0$, the qubit frequency is 5.018 GHz and the coherence times are $T_1 = 47.3 \pm 2.3$ μs and $T_{2R} = 72 \pm 7$ ns. For rapid shifting of the external flux, the device is engineered to be highly flux-sensitive. Unsurprisingly, this necessary design choice lowers coherence times compared to recently reported values for heavy-fluxonium devices [10,19,31]. We employ relatively short readout pulses of 2 μs duration to reduce decoherence errors during measurement, especially at half-flux where coherence times are shortest. With this constraint on the readout length, high readout fidelity is still achieved. Pulse generation and measurement are performed using the Quantum Instrumentation Control Kit (QICK) [32]. For further details on the experimental setup see Appendix B, and for details on qubit readout see Appendix C.

Due to the small energy splittings near half-flux and thus significant thermal population of the excited state, we implement active state preparation. We perform single-shot readout [33–35] to postselect for the ground state at Φ_a. The flux is then quickly ramped to Φ_b by applying a step pulse to the on-chip flux line (see Fig. 2). The QICK generates the step pulse with a 1 ns rising edge. The experiment concludes with a final single-shot readout at Φ_b to determine the final-state occupation probability.

To quantify the measurement fidelity we perform a π-pulse calibration experiment at $\Phi_b/\Phi_0 = 0.812$. We implement a π-pulse with a total length of 35 ns to drive population into the excited state and perform single-shot measurement. We identify the rotation angle with which to project the single-shot measurements onto a single axis with maximal contrast and determine the threshold defining the ground and excited states. This calibration achieves a single-shot fidelity of 91% which allows us to determine the measurement error rates for the ground and excited states [36]. When measuring the ground (excited) state there is 5% (4%) population in the excited (ground) state.

We incur state-preparation errors when operating near the half-flux point Φ_a. Due to excitation processes,

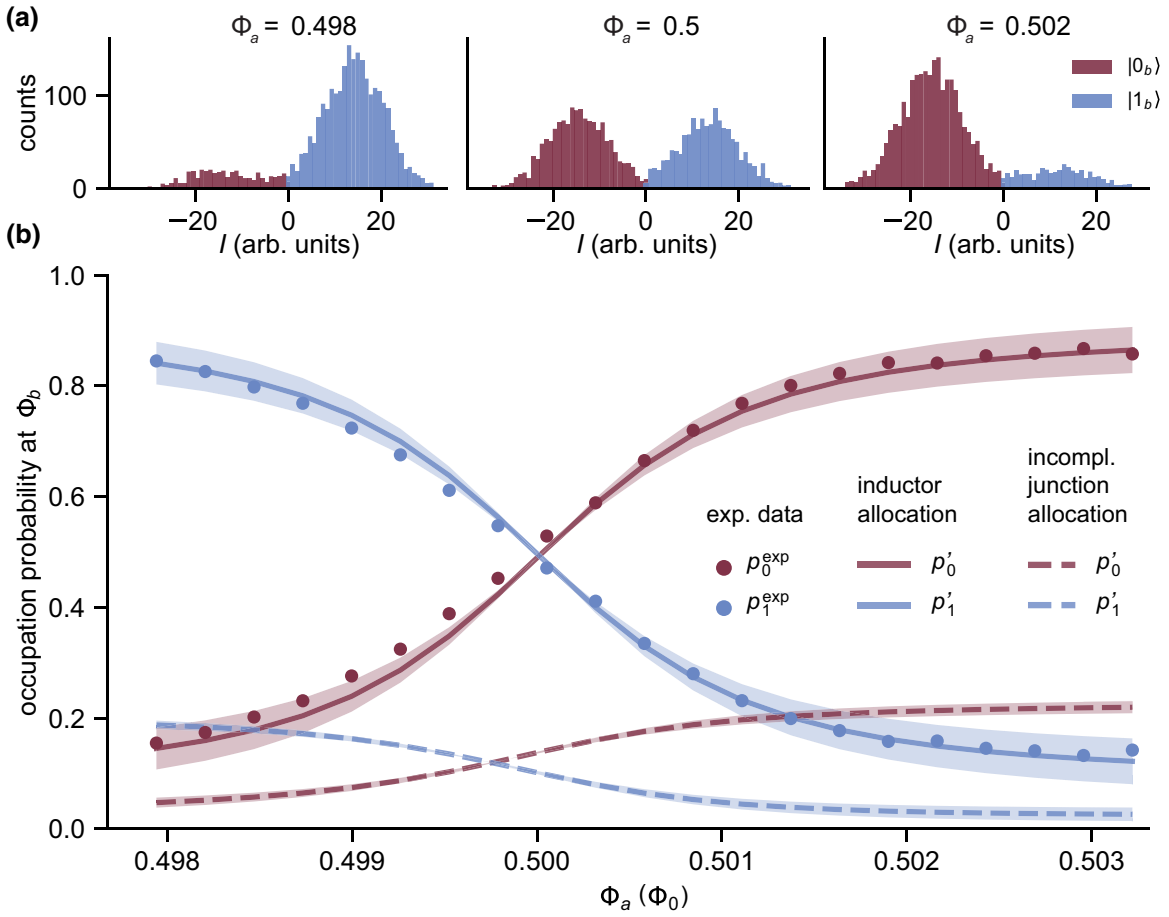

FIG. 4. Occupation probabilities $p_m = |\langle m_b|0_a\rangle|^2$ after a sudden flux ramp from initial flux $\Phi_a \in [0.498, 0.503]$ to final flux $\Phi_b = 0.812\ \Phi_0$, starting in state $|0_a\rangle$. (a) Representative single-shot data of ground state (red) and first excited state (blue) occupation probability when pulsed from $\Phi_a = 0.498, 0.5, 0.502\ \Phi_0$ to $\Phi_b = 0.812\ \Phi_0$. (b) Occupation probability as a function of initial flux point Φ_a. Points represent measured data, solid lines signify inductor allocation, and dashed lines the incomplete junction allocation. The ground (first excited) state is represented in red (blue). Experimental error bars are plotted on the data points, but are small enough to be enclosed within the size of the markers. Simulation curves are plotted accounting for measurement infidelity and state preparation errors as described in Sec. III, with $\alpha = 0.05$ as the center and shaded region showing range $\alpha \in [0.0, 0.1]$. For the inductor allocation the occupation probability primarily remains in the qubit subspace, while for incomplete junction allocation most of the occupation probability would leak into higher-lying states (not shown).

attempted initialization in the state $|0_a\rangle$ yields the mixed initial state

$$\rho = (1-\alpha)|0_a\rangle\langle 0_a| + \alpha|1_a\rangle\langle 1_a|, \tag{10}$$

where $0 \le \alpha \le 1$ denotes the preparation error. Based on the sudden approximation, the occupation probability in the state $|m_b\rangle$ is

$$p_m = (1-\alpha)|\langle m_b|0_a\rangle|^2 + \alpha|\langle m_b|1_a\rangle|^2. \tag{11}$$

Based on the total measurement time of 2 μs, a qubit thermalization time of 6 μs, and our postselection protocol, we estimate $\alpha = 0.05$. We present a range $\alpha \in [0, 0.1]$ for completeness. Additionally, we adjust the ground and excited-state occupation probabilities predicted by theory to account for the measurement infidelity from the calibration experiment:

$$\begin{pmatrix} p_0' \\ p_1' \end{pmatrix} = \begin{pmatrix} 0.95 & 0.04 \\ 0.05 & 0.96 \end{pmatrix} \begin{pmatrix} p_0 \\ p_1 \end{pmatrix}. \tag{12}$$

IV. RESULTS

From the experimental data, we determine final occupation probabilities at Φ_b as a function of Φ_a and compare these results with the simulated estimates described in Sec. II. Examples of single-shot measurements from starting external flux values of $\Phi_a/\Phi_0 = 0.498, 0.5, 0.502$ are shown in Fig. 4(a). In these measurements the single shots are distributed into two groups which align with the ground

and excited-state locations from the calibration experiment described in Sec. III.

We observe changes in occupation probability depending on the starting flux value Φ_a. When below half-flux, there is a significantly greater occupation probability of the excited state compared with the ground state. By contrast, when above half-flux, due to the change in the nature of the eigenstates the occupation probability of the ground state is greater than the first excited state. For the entire range of initial flux biases, the experimental data closely align with the predicted values obtained from the inductor allocation (or equivalently, the complete junction allocation retaining the flux-derivative term). In this allocation, the vast majority of the occupation probability (more than 98%) is predicted to remain in the ground and first excited states across all initial flux values Φ_a. By comparison, the incomplete junction allocation predicts that the majority of the occupation probability escapes from the qubit subspace. We find that the incomplete junction allocation, omitting the time-derivative term, is inconsistent with the experimental data.

V. CONCLUSION

In this work we provide experimental verification of what the flux allocation should be in the presence of rapid time-varying flux in superconducting circuits. In particular, we perform experiments applying fast flux ramps to a fluxonium circuit, designed to test the theory predictions of You *et al.* [15]. We initially bias the circuit at or near the half-flux point, then rapidly tune the flux away to a common final value, and measure the qubit occupation probability. Our experimental results closely agree with the sudden-approximation predictions using the inductor allocation. Meanwhile, the incomplete junction allocation that erroneously omits the Hamiltonian term proportional to $d\Phi/dt$ yields occupation probabilities inconsistent with the measured data. This constitutes experimental evidence supporting the theory of circuit quantization in the presence of time-dependent external flux proposed in Ref. [15]. As flux modulation of multiloop circuits becomes more prevalent, careful use of irrotational variables is essential to obtain correct predictions of device behavior.

The data that support the findings of this study are available from the corresponding author upon reasonable request.

ACKNOWLEDGMENTS

We thank Jeronimo Martinez for helpful discussions of experimental techniques. D.K.W. acknowledges support from the Army Research Office (ARO) through a QuaCGR Fellowship. S.S. is supported by the Department of Defense (DoD) through the National Defense Science & Engineering Graduate Fellowship (NDSEG) Program. Research at Princeton University and Northwestern University was funded by the ARO under Grant No. W911NF-19-10016. Devices were fabricated in the Princeton University Quantum Device Nanofabrication Laboratory (QDNL) and in the Princeton Institute for the Science and Technology of Materials (PRISM) cleanroom. J.B., D.K.W., Z.H., J.K., and A.A.H. conceived of the experiment. D.K.W., X.Y., Z.H., and J.K. developed the theory. J.B. performed design and fabrication of the device. J.B., S.S., and X.C. conducted experiments. A.A.H. advised throughout the experiment. J.B., D.K.W., X.Y., and J.K. wrote the manuscript with input from all authors.

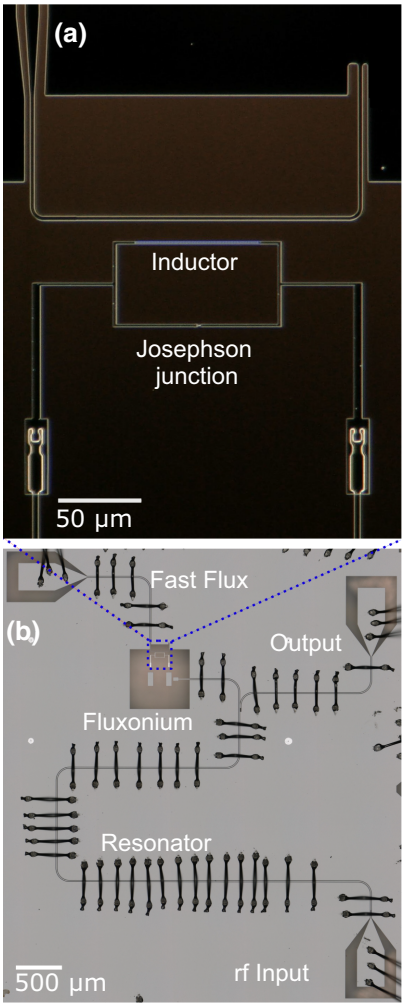

FIG. 5. Optical microscope image of the device. (b) The device has three ports for the readout resonator rf input, output, and on-chip flux bias line for driving fast flux. The dashed-outline rectangle indicates the device flux loop. (a) Dark-field optical image zoom-in on qubit flux loop. The qubit flux loop is formed by a large array of Josephson junctions in parallel with a single junction. The on-chip flux bias line used to source external flux runs near the loop and dumps current to the ground plane of the chip.

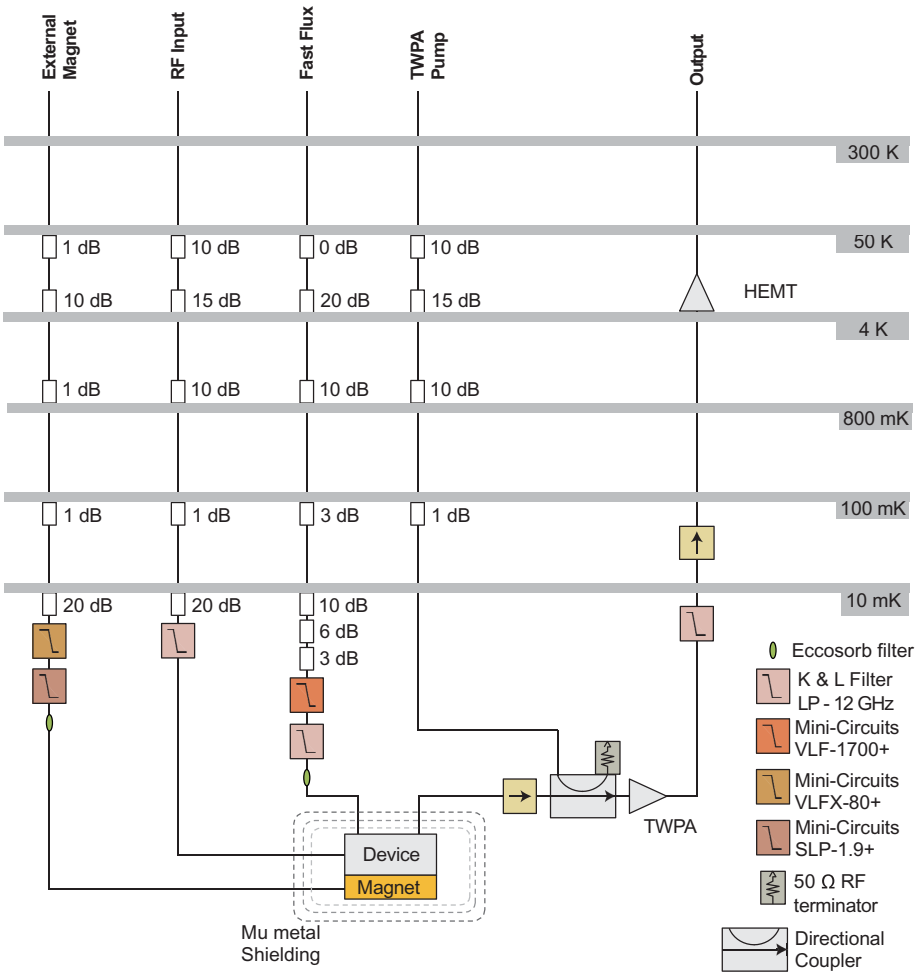

FIG. 6. Internal wiring of the dilution refrigerator. Four input lines were used: an external magnet line, an rf input to the device which was used for driving both the qubit and the cavity, a fast flux drive line to the on-chip flux bias line, and a TWPA pump input. In addition, one output line was used to read out the qubit.

The authors declare no competing financial or nonfinancial interests.

APPENDIX A: DEVICE

The device, a fluxonium qubit capacitively coupled to a half-wave CPW resonator, was fabricated on a 7 mm by 7 mm chip with 200 nm of tantalum deposited on sapphire (see Fig. 5). The readout cavity was measured in transmission via the rf input and output. The measured qubit and cavity parameters were $E_J/h = 6.49$ GHz, $E_C/h = 0.755$ GHz, $E_L/h = 0.445$ GHz, cavity frequency 7.39 GHz and linewidth 400 kHz. The qubit and cavity were coupled with a coupling strength of 110 MHz. An on-chip flux bias line was positioned near the flux loop of the fluxonium, dumping current to the ground plane of the device as seen in Fig. 5(a). The flux loop of the qubit was designed to be large and close to the flux bias line to enable the large shifts in external flux required to perform the experiment.

APPENDIX B: EXPERIMENTAL SETUP

The device was cooled and measured in a Bluefors LD-250 dilution refrigerator reaching a base temperature of 15 mK. A diagram of the internal setup of the fridge is shown in Fig. 6. To perform the experiment, four fridge input lines were needed: an rf drive input, a dc flux control, a fast flux line, and a pump line for the traveling wave parametric amplifier (TWPA). Only a single fridge output line was used. The rf input line was used for addressing both the qubit and the readout resonator. The dc flux control line was used to supply current to the external magnet for the device. The fast flux line was used to rapidly ramp the external flux on the device via the on-chip flux bias line.

A schematic of the room-temperature equipment is shown in Fig. 7. In principle, the QICK ZCU216 board can directly synthesize and down-convert signals of up to 10 GHz [37]. However, we chose to externally mix the readout resonator drive since the QICK ZCU216 features were

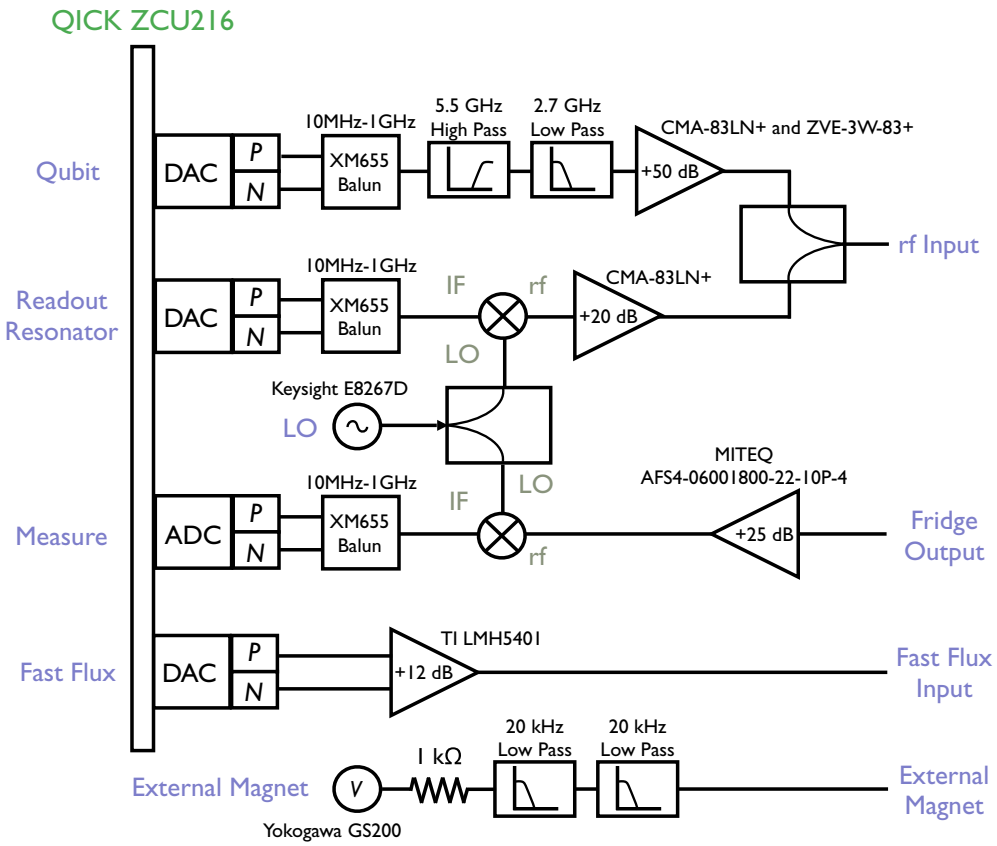

FIG. 7. Measurement equipment. Time-domain measurements were performed using the QICK ZCU216 board [37]. The QICK was used to generate all drive pulses and to read out the device. A dc voltage supply was used to control the external magnet.

still being prototyped at the time this experiment was conducted. The QICK was used to send rf signals addressing the qubit and cavity, drive fast flux, and also to read out the cavity. A separate dc voltage supply was used to control the device's external magnet.

APPENDIX C: READOUT OPTIMIZATION

In order to precisely measure the qubit population, high-fidelity readout was needed. Given the qubit's low coherence time at half-flux, the readout time needed to be relatively short in order to perform accurate postselection. The readout was optimized by measuring the readout fidelity as a function of the readout cavity drive power and frequency for a range of readout times [32]. The drive power to the resonator was chosen low enough such that the qubit state was unaffected, not operating in the "bare cavity" regime, and quantum nondemolition measurement was performed [34]. A TWPA was used to enhance the readout fidelity. The reported readout fidelity of 91% was limited by state preparation and measurement error, in particular the error due to limited readout amplification and limited analog-to-digital sampling rate (384 MHz) from the version of the QICK firmware that was used [38].

[1] F. Beaudoin, M. P. da Silva, Z. Dutton, and A. Blais, First-order sidebands in circuit QED using qubit frequency modulation, Phys. Rev. A **86**, 022305 (2012).
[2] J. D. Strand, M. Ware, F. Beaudoin, T. A. Ohki, B. R. Johnson, A. Blais, and B. L. T. Plourde, First-order sideband transitions with flux-driven asymmetric transmon qubits, Phys. Rev. B **87**, 220505(R) (2013).
[3] D. C. McKay, S. Filipp, A. Mezzacapo, E. Magesan, J. M. Chow, and J. M. Gambetta, Universal Gate for Fixed-Frequency Qubits via a Tunable Bus, Phys. Rev. Appl. **6**, 064007 (2016).
[4] P. Mundada, G. Zhang, T. Hazard, and A. Houck, Suppression of Qubit Crosstalk in a Tunable Coupling Superconducting Circuit, Phys. Rev. Appl. **12**, 054023 (2019).
[5] Y. Lu, S. Chakram, N. Leung, N. Earnest, R. K. Naik, Z. Huang, P. Groszkowski, E. Kapit, J. Koch, and D. I. Schuster, Universal Stabilization of a Parametrically Coupled Qubit, Phys. Rev. Lett. **119**, 150502 (2017).
[6] Z. Huang, Y. Lu, E. Kapit, D. I. Schuster, and J. Koch, Universal stabilization of single-qubit states using a tunable coupler, Phys. Rev. A **97**, 062345 (2018).
[7] J. A. Valery, S. Chowdhury, G. Jones, and N. Didier, Dynamical Sweet Spot Engineering via Two-Tone Flux Modulation of Superconducting Qubits, PRX Quantum **3**, 020337 (2022).

[8] P. S. Mundada, A. Gyenis, Z. Huang, J. Koch, and A. A. Houck, Floquet-Engineered Enhancement of Coherence Times in a Driven Fluxonium Qubit, Phys. Rev. Appl. **14**, 054033 (2020).

[9] Z. Huang, P. S. Mundada, A. Gyenis, D. I. Schuster, A. A. Houck, and J. Koch, Engineering Dynamical Sweet Spots to Protect Qubits from $1/f$ Noise, Phys. Rev. Appl. **15**, 034065 (2021).

[10] H. Zhang, S. Chakram, T. Roy, N. Earnest, Y. Lu, Z. Huang, D. K. Weiss, J. Koch, and D. I. Schuster, Universal Fast-Flux Control of a Coherent, Low-Frequency Qubit, Phys. Rev. X **11**, 011010 (2021).

[11] Y. Chen, K. N. Nesterov, V. E. Manucharyan, and M. G. Vavilov, Fast Flux Entangling Gate for Fluxonium Circuits, Phys. Rev. Appl. **18**, 034027 (2022).

[12] I. N. Moskalenko, I. S. Besedin, I. A. Simakov, and A. V. Ustinov, Tunable coupling scheme for implementing two-qubit gates on fluxonium qubits, Appl. Phys. Lett. **119**, 194001 (2021).

[13] I. N. Moskalenko, I. A. Simakov, N. N. Abramov, A. A. Grigorev, D. O. Moskalev, A. A. Pishchimova, N. S. Smirnov, E. V. Zikiy, I. A. Rodionov, and I. S. Besedin, High fidelity two-qubit gates on fluxoniums using a tunable coupler, npj Quantum Inf. **8**, 130 (2022).

[14] D. K. Weiss, H. Zhang, C. Ding, Y. Ma, D. I. Schuster, and J. Koch, Fast High-Fidelity Gates for Galvanically-Coupled Fluxonium Qubits Using Strong Flux Modulation, PRX Quantum **3**, 040336 (2022).

[15] X. You, J. A. Sauls, and J. Koch, Circuit quantization in the presence of time-dependent external flux, Phys. Rev. B **99**, 174512 (2019).

[16] R. P. Riwar and D. P. DiVincenzo, Circuit quantization with time-dependent magnetic fields for realistic geometries, npj Quantum Inf. **8**, 36 (2022).

[17] R. N. Rajmohan, A. Kenawy, and D. DiVincenzo, Circuit quantization with time-dependent flux:the parallel-plate SQUID (2022), ArXiv:2201.01945.

[18] J. Koch, V. Manucharyan, M. H. Devoret, and L. I. Glazman, Charging Effects in the Inductively Shunted Josephson Junction, Phys. Rev. Lett. **103**, 217004 (2009).

[19] L. B. Nguyen, Y.-H. Lin, A. Somoroff, R. Mencia, N. Grabon, and V. E. Manucharyan, High-Coherence Fluxonium Qubit, Phys. Rev. X **9**, 041041 (2019).

[20] E. A. Sete, M. J. Reagor, N. Didier, and C. T. Rigetti, Charge- and Flux-Insensitive Tunable Superconducting Qubit, Phys. Rev. Appl. **8**, 024004 (2017).

[21] S. Spilla, F. Hassler, A. Napoli, and J. Splettstoesser, Dephasing due to quasiparticle tunneling in fluxonium qubits: A phenomenological approach, New J. Phys. **17**, 065012 (2015).

[22] M. H. Devoret, in *Quantum Fluctuations: Les Houches Session LXIII*, edited by S. Reynaud, E. Giacobino, and J. Zinn-Justin (Elsevier, Amsterdam, 1997), p. 351.

[23] U. Vool and M. Devoret, Introduction to quantum electromagnetic circuits, Int. J. Circuit Theory Appl. **45**, 897 (2017).

[24] T. P. Orlando, J. E. Mooij, L. Tian, C. H. van der Wal, L. S. Levitov, S. Lloyd, and J. J. Mazo, Superconducting persistent-current qubit, Phys. Rev. B **60**, 15398 (1999).

[25] H. Goldstein, *Classical Mechanics* (Addison-Wesley, MA, 1980), 13.

[26] J. J. Sakurai and J. Napolitano, *Modern Quantum Mechanics*, 2nd ed. (Cambridge University Press, 2017) Chap. 5, p. 345.

[27] P. Groszkowski and J. Koch, Scqubits: A Python package for superconducting qubits, Quantum **5**, 583 (2021).

[28] G. Zhu, D. G. Ferguson, V. E. Manucharyan, and J. Koch, Circuit QED with fluxonium qubits: Theory of the dispersive regime, Phys. Rev. B **87**, 024510 (2013).

[29] T. C. White, J. Y. Mutus, I. C. Hoi, R. Barends, B. Campbell, Y. Chen, Z. Chen, B. Chiaro, A. Dunsworth, E. Jeffrey, J. Kelly, A. Megrant, C. Neill, P. J. O'Malley, P. Roushan, D. Sank, A. Vainsencher, J. Wenner, S. Chaudhuri, J. Gao, and J. M. Martinis, Traveling wave parametric amplifier with Josephson junctions using minimal resonator phase matching, Appl. Phys. Lett. **106**, 242601 (2015).

[30] D. I. Schuster, A. Wallraff, A. Blais, L. Frunzio, R.-S. Huang, J. Majer, S. M. Girvin, and R. J. Schoelkopf, AC Stark Shift and Dephasing of a Superconducting Qubit Strongly Coupled to a Cavity Field, Phys. Rev. Lett. **94**, 123602 (2005).

[31] A. Somoroff, Q. Ficheux, R. A. Mencia, H. Xiong, R. V. Kuzmin, and V. E. Manucharyan, Millisecond coherence in a superconducting qubit, **1** (2021), ArXiv:2103.08578.

[32] L. Stefanazzi, K. Treptow, N. Wilcer, C. Stoughton, C. Bradford, S. Uemura, S. Zorzetti, S. Montella, G. Cancelo, S. Sussman, A. Houck, S. Saxena, H. Arnaldi, A. Agrawal, H. Zhang, C. Ding, and D. I. Schuster, The QICK (Quantum Instrumentation Control Kit): Readout and control for qubits and detectors, Rev. Sci. Instrum. **93**, 044709 (2022).

[33] F. Mallet, F. R. Ong, A. Palacios-Laloy, F. Nguyen, P. Bertet, D. Vion, and D. Esteve, Single-shot qubit readout in circuit quantum electrodynamics, Nat. Phys. **5**, 791 (2009).

[34] Y. Y. Gao, M. A. Rol, S. Touzard, and C. Wang, Practical guide for Building Superconducting Quantum Devices, PRX Quantum **2**, 040202 (2021).

[35] D. Ristè, C. C. Bultink, K. W. Lehnert, and L. DiCarlo, Feedback Control of a Solid-State Qubit Using High-Fidelity Projective Measurement, Phys. Rev. Lett. **109**, 240502 (2012).

[36] T. Walter, P. Kurpiers, S. Gasparinetti, P. Magnard, A. Potočnik, Y. Salathé, M. Pechal, M. Mondal, M. Oppliger, C. Eichler, and A. Wallraff, Rapid High-Fidelity Single-Shot Dispersive Readout of Superconducting Qubits, Phys. Rev. Appl. **7**, 054020 (2017).

[37] S. Uemura, L. Stefanazzi, K. Treptow, N. Wilcer, C. Stoughton, M. Di Federico, S. Sussman, D. Schuster, A. Agrawal, H. Zhang, C. Ding, K. Nowrouzi, N. Fruitwala, G. Huang, A. Butko, Y. Xu, C. Guinn, and A. Houck, QICK (Quantum Instrumentation Control Kit): Progress on an open-source qubit controller, Bulletin of the American Physical Society (2023).

[38] QICK Github repository, https://github.com/openquantumhardware/qick (2023).